

Article

High-Pressure Elastic, Vibrational and Structural Study of Monazite-Type GdPO_4 from Ab Initio Simulations

Alfonso Muñoz *  and Placida Rodríguez-Hernández 

Departamento de Física, Instituto de Materiales y Nanotecnología, MALTA Consolider Team, Universidad de La Laguna, La Laguna, 38200 Tenerife, Spain; plrguez@ull.edu.es

* Correspondence: amunoz@ull.edu.es; Tel.: +34-922-318-275

Received: 19 April 2018; Accepted: 8 May 2018; Published: 10 May 2018



Abstract: The GdPO_4 monazite-type has been studied under high pressure by first principles calculations in the framework of density functional theory. This study focuses on the structural, dynamical, and elastic properties of this material. Information about the structure and its evolution under pressure, the equation of state, and its compressibility are reported. The evolution of the Raman and Infrared frequencies, as well as their pressure coefficients are also presented. Finally, the study of the elastic constants provides information related with the elastic and mechanical properties of this compound. From our results, we conclude that monazite-type GdPO_4 becomes mechanically unstable at 54 GPa; no evidence of soft phonons has been found up to this pressure at the zone center.

Keywords: ab initio; monazite; orthophosphate; equation of state; elasticity; phonons; Raman

1. Introduction

The APO_4 orthophosphates compounds (A = trivalent cation) are materials analogous to orthoarsenates, orthovanadates, and orthosilicates. The size of the ionic radius of the A cation defines the two different structures where this family of compounds crystallizes. APO_4 compounds with an ionic radius lower than Gd crystallize in the tetragonal zircon structure ($I4_1/amd$, space group 141 with $Z = 4$). All other orthophosphates ($A = \text{La}$ to Gd) crystallize into a monoclinic lower symmetry phase, that is, a monazite structure ($P2_1/n$, space group 14 with $Z = 4$) [1]. The monazite structure is isostructural to cerium phosphate mineral (monazite). This structure can be viewed as being composed by alternating edge-sharing AO_9 polyhedra, with a structural distortion derived from a rotation of the PO_4 tetrahedra and a lateral shift of the (100) planes that reduce the symmetry from the tetragonal of the zircon structure to the monoclinic symmetry.

Due to their numerous potential applications, the orthophosphate family has attracted a lot of interest in the last decades. The study of the mechanical properties of these materials can be relevant, since some orthophosphates have shown to be promising materials for oxidation-resistant ceramic toughening [2] and to have interesting luminescent and optical properties with a wide range of potential applications [3–6].

This family of minerals appears in nature as accessory mineral in rhyolites and granitoid rocks [1]. Therefore, the study of orthophosphates may be of importance in petrology [7], chemistry, and mineral physics. These materials can be employed as geochronometers for geological dating [8], because of their doping with radioactive elements that possess a very large half-life. Additionally, since orthophosphates incorporate rare earth elements, they can also be used to determine the distribution of rare earth elements in our Planet [9]. Another interesting application of these compounds is related to their use as potential matrix for nuclear waste disposal [5,10–12]. GdPO_4 and

other orthophosphates have been suggested as inclusion compounds to make nuclear fuel canisters due to their high neutron absorption [13]. Therefore, the study of these orthophosphates under high pressure is very promising for future practical applications. Although there are several studies focused on pressure-induced transition and on the structural and vibrational properties of monazite phosphates under pressure [7,14–18], these studies were carried out only up to 30 GPa. A systematic understanding of their properties has not yet been achieved; the study of their elastic and mechanical properties is scarce [5,19,20]. Clearly, additional researches are needed to deepen our knowledge of this group of materials. A systematic investigation of the properties of monazite phosphates (particularly at high pressure) is necessary, especially if we want to use them in efficient and safe applications.

The ab initio methods have been successfully applied to study the thermodynamic properties of monazite rare earth orthophosphates [21–24]. Moreover, the use of ab initio simulations has become a strong and very well supported method to investigate the properties of materials under high pressures [25–28]. In particular, in the case of monazite-type orthophosphates under pressure, the ab initio simulations have been employed with good results [29,30].

The aim of the present paper is to contribute to the knowledge of the properties of orthophosphates at high pressure. In this work, we perform a detailed study of the structural, dynamic, and elastic properties of monazite-type GdPO_4 under pressures up to 60 GPa, going from first principles simulations. This method has proven to be quite efficient, in order to study a variety of properties on related compounds.

2. Simulations Details

The influence of pressure on the crystal structure, mechanical and vibrational properties of monazite-type GdPO_4 has been analyzed using ab initio simulations. The study was based on the Density Functional Theory (DFT) [31] employing the Vienna Ab initio Simulation Package (VASP) [32–34] and pseudopotentials generated with the Projector-Augmented Wave scheme (PAW) [35,36], with the f electrons included into the core. This has proven to give good results in the study of monazite-type structures [20,30,37]. To reach accurate results, the set of plane waves was extended up to a 520-eV cutoff energy and the exchange-correlation energy was expressed by means of the Generalized-Gradient Approximation (GGA) with the Perdew-Burke-Ernzerhof for solids (PBEsol) functional [38]. A dense grid of Monkhorst-Pack [39] k-special points was utilized to perform the integrations on the Brillouin Zone (BZ). The achieved convergence was 1 meV per formula unit in the total energy. All the structural parameters were optimized by minimizing the forces on the atoms and the stress tensor, at selected volumes. This method has been successfully applied to study the phase stability, and structural properties of semiconductors under high pressure [40]. To carry out the study of the mechanical properties of GdPO_4 , we have evaluated the elastic constants, which describe the mechanical properties of a material in the region of small deformations. The elastic constants can be obtained by computing the macroscopic stress of a small strain with the use of the stress theorem [41,42]. In the present study, we employ the method implemented in the VASP code: the ground state and fully optimized structures were strained in different directions taking into account their symmetry [43].

The phonons study was performed using the supercell method [44]. The diagonalization of the dynamical matrix provides the frequencies of the normal modes. Furthermore, these calculations also provide the symmetry and eigenvectors of the phonon modes at the Γ point. The calculation of the phonon dispersion curves along the main directions within the BZ was carried out with a supercell of size $2 \times 2 \times 2$. Following the conclusions of our previous studies and those of Blanca-Romero et al. [45], in all the calculations, we neglect the spin-orbit interaction, because the structural properties are barely affected [15,17,26,29,30,37].

3. Results and Discussion

3.1. Structural Properties

The monoclinic structure of monazite, space group $P2_1/n$ [1] has been described in the introduction. A schematic view of the crystal structure is presented in Figure 1. It can be seen as an alternating chain of phosphorus-oxygen PO_4 tetrahedra and trivalent cation-oxygen GdO_9 polyhedra.

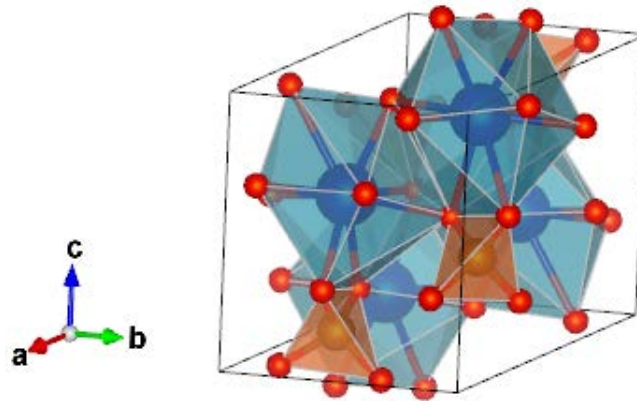


Figure 1. (Color online) Crystal structure of monazite-type GdPO_4 . Oxygen, phosphorus, and gadolinium atoms are shown in red, orange, and blue, respectively. The PO_4 tetrahedral units and the GdO_9 polyhedral units are also shown.

The calculated structural parameters and atomic coordinates at ambient pressure are given in Tables 1 and 2, and are in a very close agreement with the available theoretical and experimental results [11,14,18,20,21]. Previous theoretical results [20] differ slightly due to the exchange-correlation functional used in the calculations.

Table 1. Structural parameters of monazite-type GdPO_4 at 0 GPa.

	This Study	Experiments	Theory
a (Å)	6.6276	6.623 ^a 6.6516(3) ^b 6.62(2) ^c	6.4152 ^d 6.713 ^e
b (Å)	6.8145	6.829 ^a 6.84840(7) ^b 6.823(2) ^c	6.6103 ^d 6.887 ^e
c (Å)	6.2930	6.335 ^a 6.33571(12) ^b 6.319(2) ^c	6.0953 ^d 6.358 ^e
β (°)	104.18°	103.80 ^a 104.023(2) ^b 104.16(2) ^c	104.6 ^d 104.2 ^e

^a Reference [14]. ^b Reference [18]. ^c Reference [11]. ^d Reference [20]. ^e Reference [21]. Data from References [18,20] were obtained in a different setting than the one employed in the present work.

Table 2. Atomic positions of monazite-type GdPO_4 at 0 GPa.

Atom	Site	x	y	z
Gd	4e	0.28394	0.14513	0.08817
P	4e	0.29933	0.16215	0.61291
O ₁	4e	0.2510	0.0000	0.4330
O ₂	4e	0.3850	0.3381	0.5017
O ₃	4e	0.4735	0.1010	0.8184
O ₄	4e	0.1182	0.2100	0.7148

The evolution of the structural parameters with pressure is displayed in Figure 2a. The calculations have been already compared with experiments [14,18], showing an excellent agreement. The obtained linear axial compressibilities of each axis are: $K_a = \frac{-1}{a} \frac{da}{dp} = 2.76 \times 10^{-3} \text{ GPa}^{-1}$; $K_b = \frac{-1}{b} \frac{db}{dp} = 2.25 \times 10^{-3} \text{ GPa}^{-1}$; $K_c = \frac{-1}{c} \frac{dc}{dp} = 2.03 \times 10^{-3} \text{ GPa}^{-1}$. Therefore, from the present results and previous studies [14,18], it can be concluded that the compression of GdPO_4 , as in other monazite-type phosphates, is not isotropic. The a -axis is the most compressible one and the c -axis the least compressible one. As shown in Figure 2a, there is a tendency for the unit-cell parameter a to approach the value of c . Moreover, in Figure 2b, it can be seen that the monoclinic β angle decreases under compression. As a result of these two facts, there is a gradual symmetrization of the monazite structure under compression.

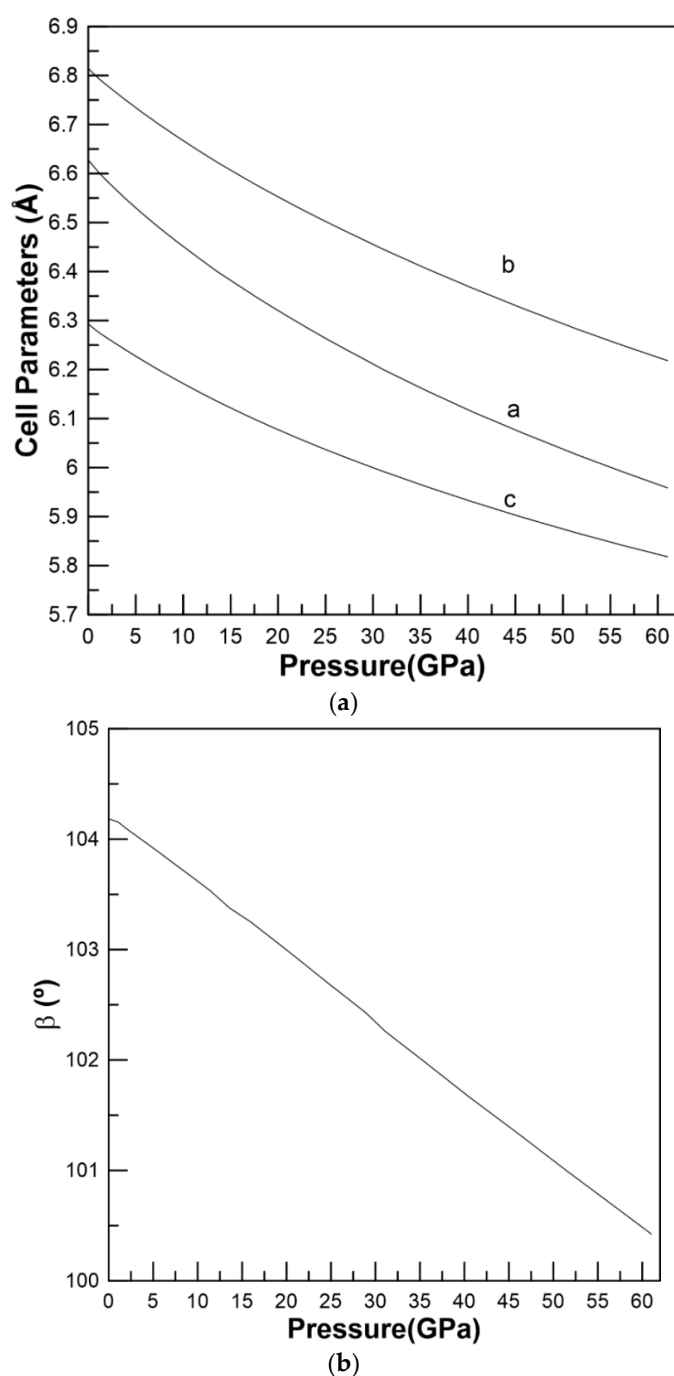


Figure 2. (a) Pressure dependence of the lattice parameters. (b) Pressure dependence of the β angle.

The bulk modulus, B_0 , and its first pressure derivative were obtained by fitting the set of theoretical energy-volume data with a third-order Birch-Murnaghan (BM) Equation of State (EOS) [46]. The results ($B_0 = 138.3$ GPa, and $B'_0 = 4.02$) are summarized in Table 3 and are compared with previous results of B_0 reported for GdPO_4 : the agreement between experiments is good.

Table 3. Volume at 0 GPa, bulk modulus, B_0 , and its pressure derivative, B'_0 , from a fit with a 3th order Birch Murnaghan EOS.

	This Work	Experiments	Theory
V (\AA^3)	275.55	279.1 ^a	250.20 ^e
		280.008(4) ^b	284.96 ^f
		276.4(4) ^c	
B_0 (GPa)	138.3	160 ^a	149 ^g
		128.1(8) ^b	121.0 ^h
		137 ^d	
B'_0	4.07	5.8(2) ^b	

^a Reference [14]. ^b Reference [18]. ^c Reference [11]. ^d Reference [47]. ^e Reference [20]. ^f Reference [21]. ^g Reference [48], ^h Reference [24].

From our calculations, we have determined the pressure dependence of the polyhedral volumes and distortions for monazite GdPO_4 . Figure 3a presents the relative volume of the PO_4 and GdO_9 polyhedra and that of the unit-cell. As it can be observed, the PO_4 tetrahedron is highly incompressible, while the GdO_9 polyhedron is much more compressible. Actually, in the monazite-type GdPO_4 , the volume change of the GO_9 polyhedra seems to be responsible for most of the volume reduction induced by pressure within the structure. In fact, the phosphate tetrahedra can be treated as a rigid unit in the monazite-type phosphate [17,18,48]. The P–O distances do not vary greatly within the tetrahedra. At zero pressure, two distances are 1.55 \AA , and the two other 1.56 \AA , and 1.54 \AA , while at 53 GPa these distances decrease to 1.51 $\text{\AA} \times 2$, 1.52 \AA , and 1.49 \AA , respectively. Indeed, the distortion index, calculated with VESTA [49], for the PO_4 polyhedron (see Figure 3b) is very small, and it increases slowly with compression. Regarding the GdO_9 polyhedra at zero pressure, the central gadolinium atom is connected to nine oxygen atoms with eight bonds whose lengths vary from 2.34 to 2.55 \AA , with one length at 2.78 \AA . At 53 GPa the lengths range from 2.16 to 2.46 \AA and the largest one changes to 2.53 \AA . The GdO_9 distortion index do not vary linearly, as seen in Figure 3b. There is a decrease around 4 GPa, followed by a considerable increase in pressure, in a similar manner than in the isostructural LaPO_4 and CePO_4 . The GdO_9 polyhedron is more distorted than the PO_4 tetrahedron: its distortion index changes from approximately 0.0381 at ambient pressure to 0.0440 at 54 GPa.

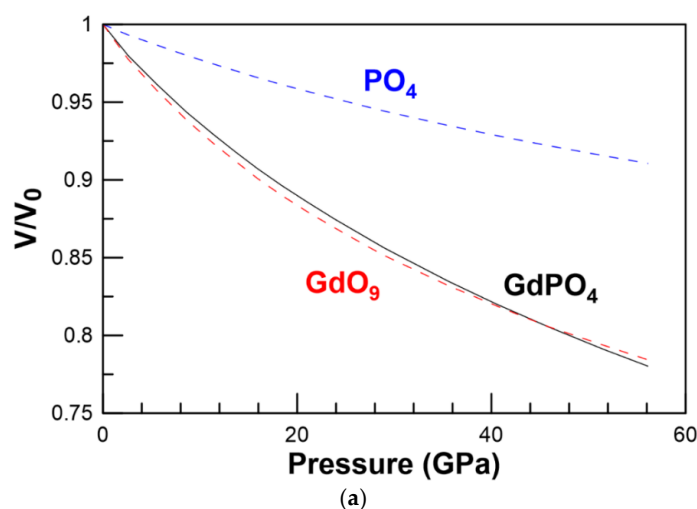


Figure 3. Cont.

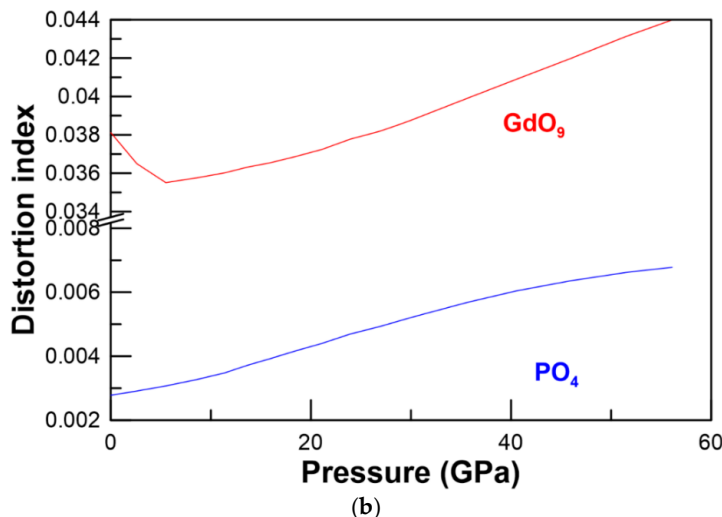


Figure 3. (Color online) (a) Relative variation with pressure of the polyhedral and unit cell volumes of monazite-type GdPO₄. (b) Distortion index of the PO₄ tetrahedron and the GdO₉ polyhedron.

3.2. Elastic Properties

GdPO₄ belongs to the monoclinic space group n° 14; it therefore has 13 independent elastic constants [50]: C₁₁, C₁₂, C₁₃, C₁₅, C₂₂, C₂₃, C₂₅, C₃₃, C₃₅, C₄₄, C₄₆, C₅₅, and C₆₆ in the Voigt notation. Table 4 summarizes our results for the set of C_{ij} elastic constants at 0 GPa. The values here reported are in overall good agreement with those of Feng et al. [20]. The diagonal elastic constants C₁₁, C₂₂, C₃₃, are the highest ones, while C₂₅, C₃₅, C₄₆ are the lowest ones. It must be noted that in [20], the cell parameters are underestimated, as commented above. When a non-zero uniform stress is applied to a crystal, the relevant magnitudes that describe their elastic properties are the elastic stiffness coefficients B_{ij} [51]. In the special case of a hydrostatic pressure, P, applied to a monoclinic crystal, the elastic stiffness coefficients are related to the elastic constants through the following relationships [51,52]:

$$B_{11} = C_{11} - P, B_{12} = C_{12} + P, B_{13} = C_{13} + P, B_{15} = C_{15}, B_{22} = C_{22} - P, B_{23} = C_{23} + P, B_{25} = C_{25}, B_{33} = C_{33} - P, B_{35} = C_{35}, B_{44} = C_{44} - P, B_{46} = C_{46}, B_{55} = C_{55} - P \text{ and } B_{66} = C_{66} - P.$$

Table 4. Elastic constants (in GPa) of monazite-type GdPO₄ at 0 GPa.

C ₁₁	C ₂₂	C ₃₃	C ₄₄	C ₅₅	C ₆₆	C ₁₂	C ₁₃	C ₁₅	C ₂₃	C ₂₅	C ₃₅	C ₄₆
262.19	251.61	205.01	65.19	60.32	58.16	71.41	90.99	5.28	88.50	−18.17	−18.17	−13.70

Figure 4 shows the pressure dependence of the elastic stiffness coefficients, B_{ij}. It can be seen that, B₁₁, B₂₂, B₃₃, B₁₂, B₁₃, and B₂₃ increase with pressure in the whole pressure range studied, especially in the diagonal components, while B₄₄, B₅₅ and B₆₆ decrease under compression. On the other hand, B₁₅ is almost unaffected by pressure. It should be noted that B₂₅, B₃₅, B₄₆ have similar negatives values and that they decrease under compression.

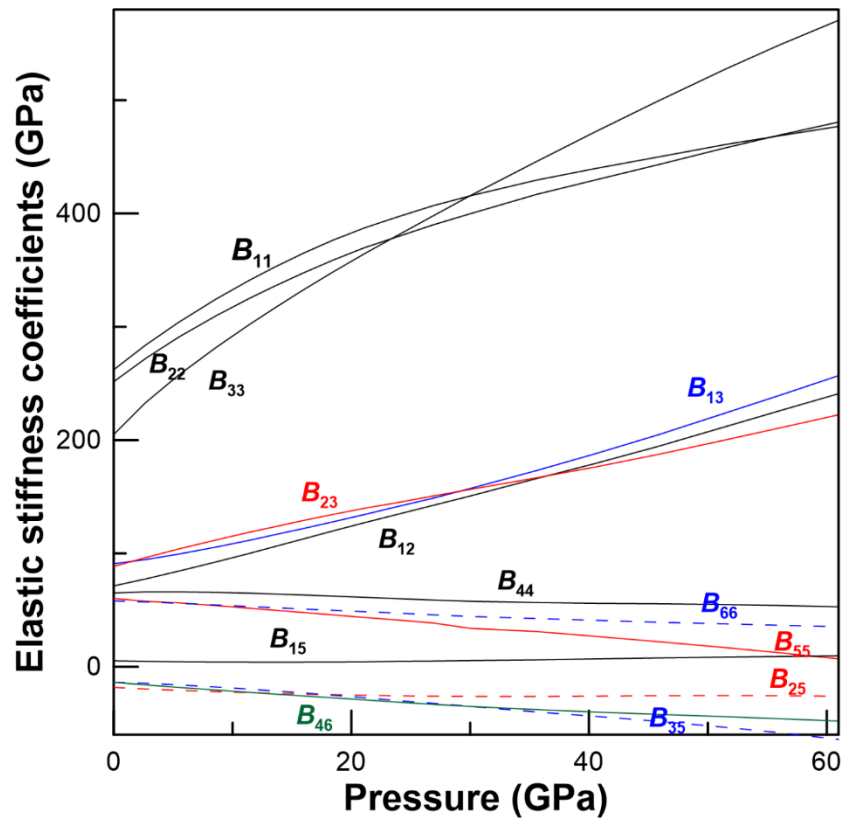


Figure 4. (Color online) Pressure evolution of the elastic stiffness coefficients, B_{ij} .

At zero pressure, a crystal is mechanically stable when the Born stability criteria are fulfilled [53]. However, when a hydrostatic pressure is applied to the crystal, the generalized Born stability criteria [52,54] must be employed to study the mechanical stability. This means that the matrix B_{ij} must be positive definite. Consequently, the stability conditions for a monoclinic crystal are given by the following conditions:

$$M_1 = B_{11} > 0$$

$$M_2 = B_{11}B_{22} - B_{12}^2 > 0$$

$$M_3 = (B_{22}B_{33} - B_{23}^2)B_{11} - B_{33}B_{12}^2 + 2B_{23}B_{12}B_{13} - B_{22}B_{13}^2 > 0$$

$$M_4 = B_{44} > 0$$

$$M_5 = B_{12}^2 B_{35}^2 - B_{33} B_{55} B_{12}^2 + 2B_{55} B_{12} B_{13} B_{23} - 2B_{12} B_{13} B_{25} B_{35} \\ - 2B_{12} B_{15} B_{23} B_{35} + 2B_{33} B_{12} B_{15} B_{25} + B_{13}^2 B_{25}^2 - B_{22} B_{55} B_{13}^2 \\ - 2B_{13} B_{15} B_{23} B_{25} + 2B_{22} B_{13} B_{15} B_{35} + B_{15}^2 B_{23}^2 - B_{22} B_{33} B_{15}^2 \\ - B_{11} B_{55} B_{23}^2 + 2B_{11} B_{23} B_{25} B_{35} - B_{11} B_{33} B_{25}^2 - B_{11} B_{22} B_{35}^2 \\ + B_{11} B_{22} B_{33} B_{55} > 0$$

$$M_6 = B_{44} B_{66} - B_{46}^2 > 0$$

The simulations of the elastic constants have been extended up to 60 GPa, well above the maximum experimental pressure reported [14,15]. The generalized stability criteria for GdPO₄ as function of the pressure are presented in Figure 5. At 54 GPa, one of the M_6 criterion is violated, making the system mechanically unstable at this pressure. No evidence of soft phonons was found at the Γ point in this pressure range. These results are consistent with the experimental and theoretical reports that confirm that there is no phase transition induced by pressure in the monazite structure up to the highest pressure reached in those studies (30 GPa) [14,17].

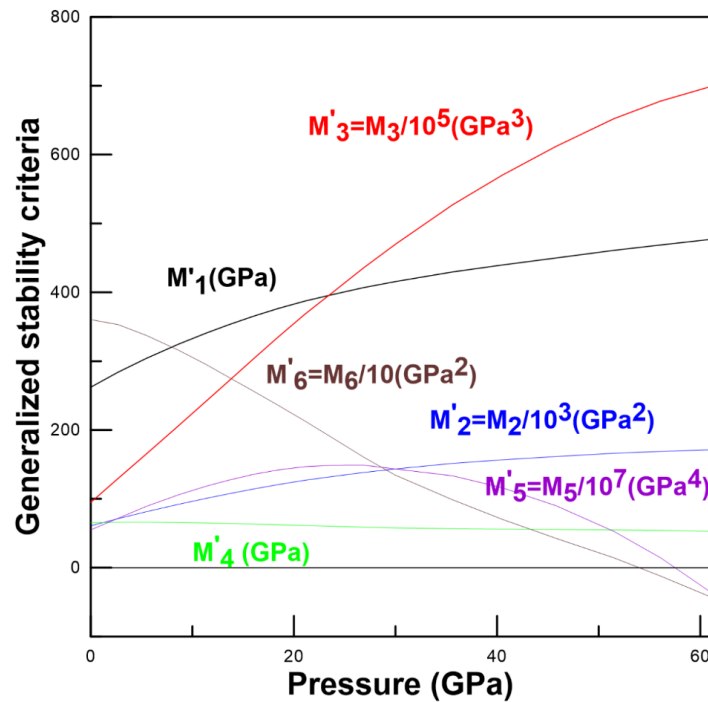


Figure 5. (Color online) Generalized stability criteria for monazite-type GdPO_4 .

The bulk modulus (B), the shear modulus (G), the Young modulus (E), and the Poisson's ratio (ν) describe the major elastic properties of a material. Analytical expressions can be obtained for these moduli in the Voigt, Reuss and Hill approximations [55–57] from the elastic stiffness coefficients, B_{ij} . Hill has proved that the Voigt and Reuss approximations are limits and pointed out that the arithmetic mean of the two bounds can be considered as the actual B and G elastic moduli. In the case of a monoclinic crystal, the bulk and shear moduli can be expressed in the three approximations as [58]:

$$B_V = \frac{B_{11} + B_{22} + B_{33} + 2(B_{12} + B_{23} + B_{13})}{9}$$

$$\frac{1}{B_R} = S_{11} + S_{22} + S_{33} + 2(S_{12} + S_{23} + S_{13})$$

$$B_H = \frac{B_V + B_R}{2}$$

$$G_V = \frac{B_{11} + B_{22} + B_{33} - (B_{12} + B_{23} + B_{13}) + 3(B_{44} + B_{55} + B_{66})}{15}$$

$$\frac{1}{G_R} = \frac{4(S_{11} + S_{22} + S_{33}) - 4(S_{12} + S_{23} + S_{13}) + 3(S_{44} + S_{55} + S_{66})}{15}$$

$$G_H = \frac{G_V + G_R}{2}$$

where S_{ij} refers to components of the elastic compliances tensor, and subscripts V , R , and H stand for Voigt, Reuss and Hill respectively. The Young modulus, E , and the Poisson's ratio, ν , are obtained with the expressions [59]:

$$E_X = \frac{9B_X G_X}{G_X + 3B_X}$$

$$\nu_X = \frac{1}{2} \left(\frac{3B_X - 2G_X}{3B_X + G_X} \right)$$

where the subscript X refers to the symbols V , R , and H .

In order to discuss the elastic properties of GdPO_4 at ambient pressure, the elastic moduli at 0 GPa are summarized in Table 5. The bulk modulus, $B_H = 134.47$ GPa is in rather good agreement with our theoretical value of $B_0 = 138.3$ GPa, obtained from a fit with a third order Birch-Murnaghan equation of state [46], and with the experimental values of $B_0 = 137$ GPa previously reported [47]. As for E , G , and B/G elastic moduli, as well as the Poisson's ratio, ν , at zero applied pressure, it should be noted once more that there is good agreement between our calculations and the experimental results. These facts demonstrate the quality of our simulations.

Table 5. Elastic moduli B , E and G , the B/G ratio, and the Poisson's ratio, ν , in the Hill approximation, at 0 GPa.

B_H (GPa)	E_H (GPa)	G_H (GPa)	B_H/G_H	ν
134.47 ^a	169.62 ^a	65.575 ^a	2.05 ^a	0.289 ^a
137 ^b	172 ^b	67 ^b	2.045 ^b	0.290 ^b
121.0 ^c	165.2 ^c	64.9 ^c	1.86 ^c	

^a This work, ^b Reference [47], ^c Reference [24].

The pressure dependence of the elastic moduli up to 56.1 GPa is presented in Figure 6a–d. It can be observed that B_H , and ν_H increase with pressure. However, E_H and G_H increase under compression reaching maximum values at 11 GPa and 9 GPa, respectively; above that pressure they decrease. All the elastic moduli change dramatically around 54 GPa, since the monazite structure becomes mechanically unstable. The Poisson's ratio gives information about the characteristics of the bonding forces and the chemical bonding. The value of the Poisson's ratio in the Hill approximation is $\nu_H = 0.29$ at 0 GPa. A value of $\nu > 0.25$ indicates that the interatomic bonding forces are predominantly central and that ionic bonding is predominant against covalent bonding [60,61]. The increase of ν upon pressure can be interpreted as an increase of the metallization.

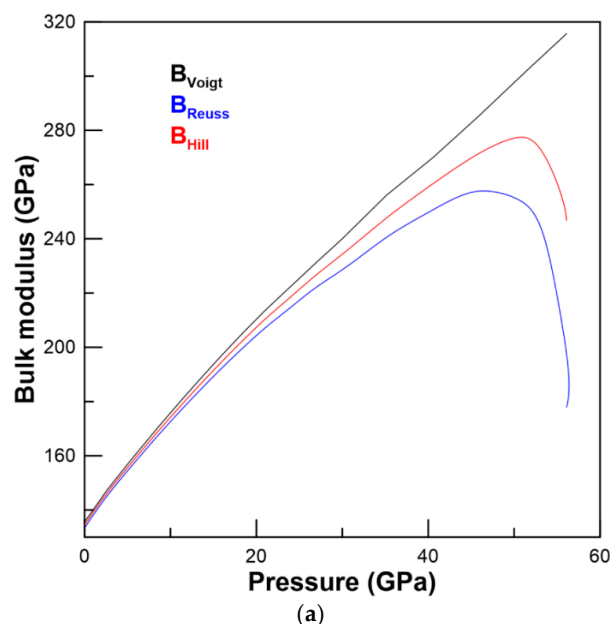


Figure 6. Cont.

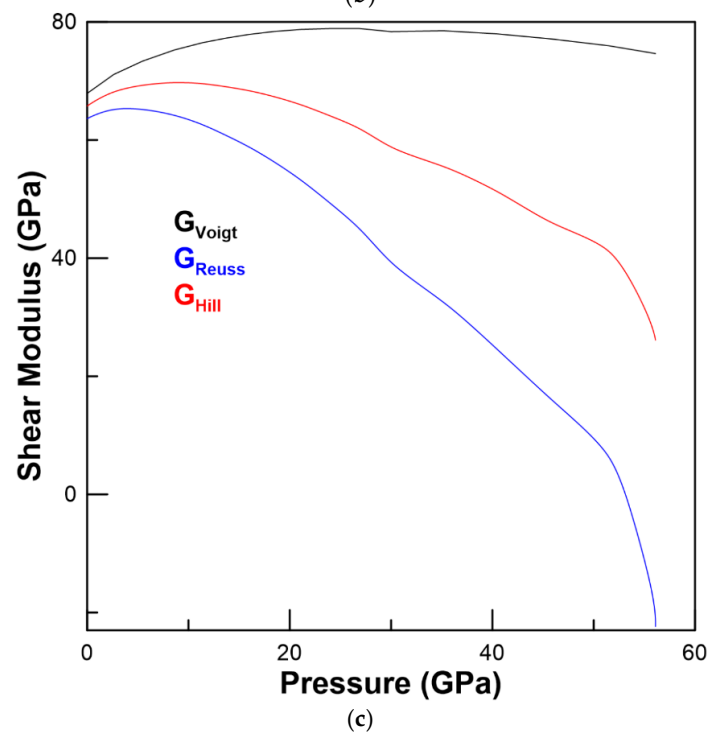
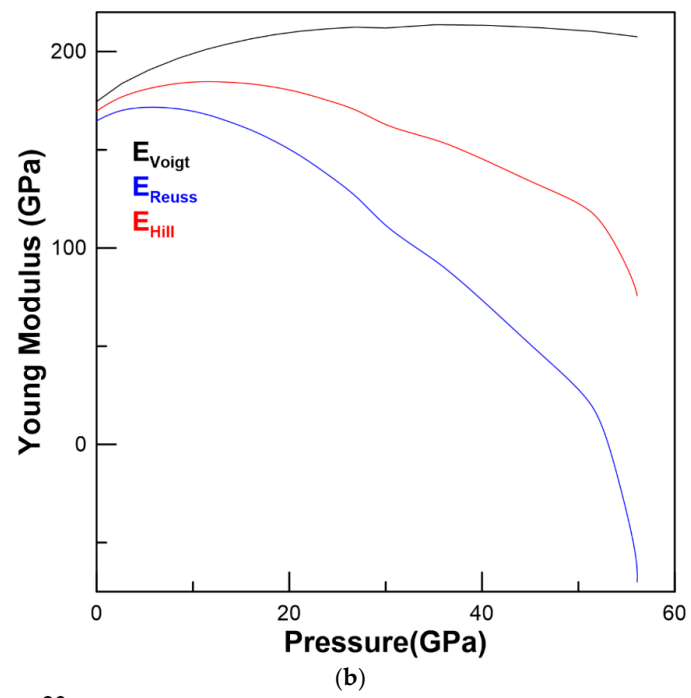


Figure 6. Cont.

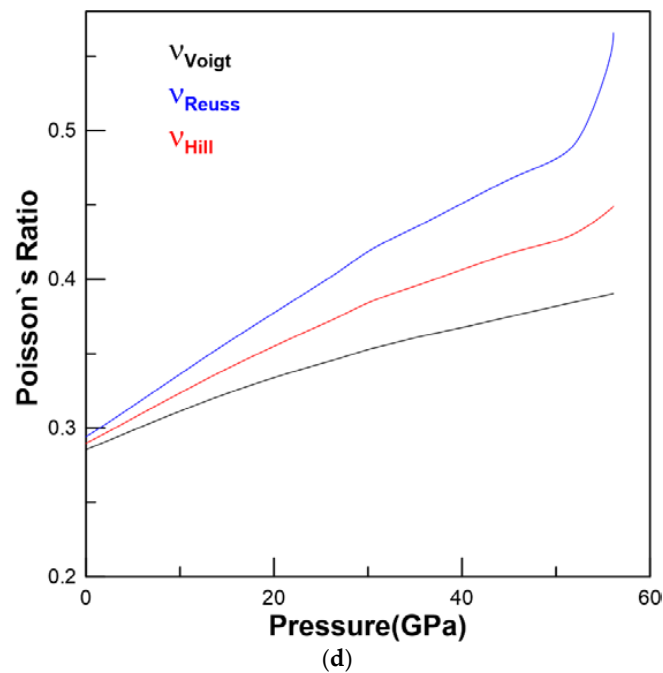


Figure 6. (Color online) (a) Pressure dependence of the bulk modulus, B . (b) Pressure dependence of the Young modulus, E . (c) Pressure dependence of the shear modulus, G . (d) Pressure dependence of the Poisson's, ν , in the approximation of Voigt, Reuss and Hill.

The B/G ratio is 2.05 and it increases with pressure (see Figure 7). Therefore, GdPO_4 monazite is more resistant to volume compression than to shear deformation ($B > G$). Moreover, according to Pugh criterion, monazite-type GdPO_4 behaves like a ductile material, since B/G is smaller than 1.75 [62], in the whole pressure range studied (materials with $B/G < 1.75$ behave as brittle materials). Our B/G value is consistent with the experimental result of Du et al. [47], although it is somewhat larger than the theoretical one of reference [24]. This is probably due to the small value of B_0 reported in that reference. However, it is clear that monazite GdPO_4 is a ductile material.

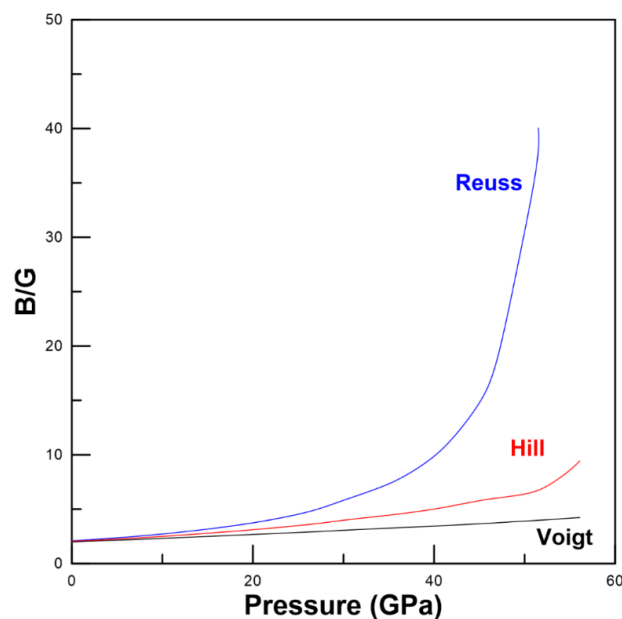


Figure 7. (Color online) Pressure dependence of the B/G ratio.

3.3. Vibrational Properties

The phonon dispersion of GdPO_4 along the main paths on the Brillouin zone is presented in Figure 8. Three frequency regions are separated by two gaps: a little one between the low- and the medium-frequency regions, and a bigger one between the medium- and the high-frequencies regions. The Partial Density Of States (PDOS) for phonons (see Figure 9) allows us to analyze these vibrations. The PDOS presents three zones separated by two gaps. The first zone, corresponding to the low-frequencies, down to 311 cm^{-1} , is composed of vibrations of Gd atoms and GdO_9 polyhedra, as well as a small contribution of PbO_4 tetrahedra. The intermediate-frequency zone, from 381 cm^{-1} to 600 cm^{-1} , is mainly due to vibrations of the PbO_4 tetrahedra with a very small contribution from the GdO_9 polyhedra. A large gap of $\approx 340 \text{ cm}^{-1}$ separates this zone with the high-frequency region, which corresponds to frequencies between 942 cm^{-1} and 1073 cm^{-1} that are only due to vibrations from PbO_4 units. Therefore, the vibrational spectra of the GdPO_4 monazite could be interpreted in term of the modes of the PbO_4 tetrahedra, which can be considered as independent units in the monazite structure, and GdO_9 polyhedra. Indeed, the vibrational spectrum of monazites ABO_4 has been interpreted in terms of internal modes (bending and stretching modes) associated with the tetrahedron BO_4 and external modes (translational and rotational) which involves movement of both A and BO_4 ions [17,63].

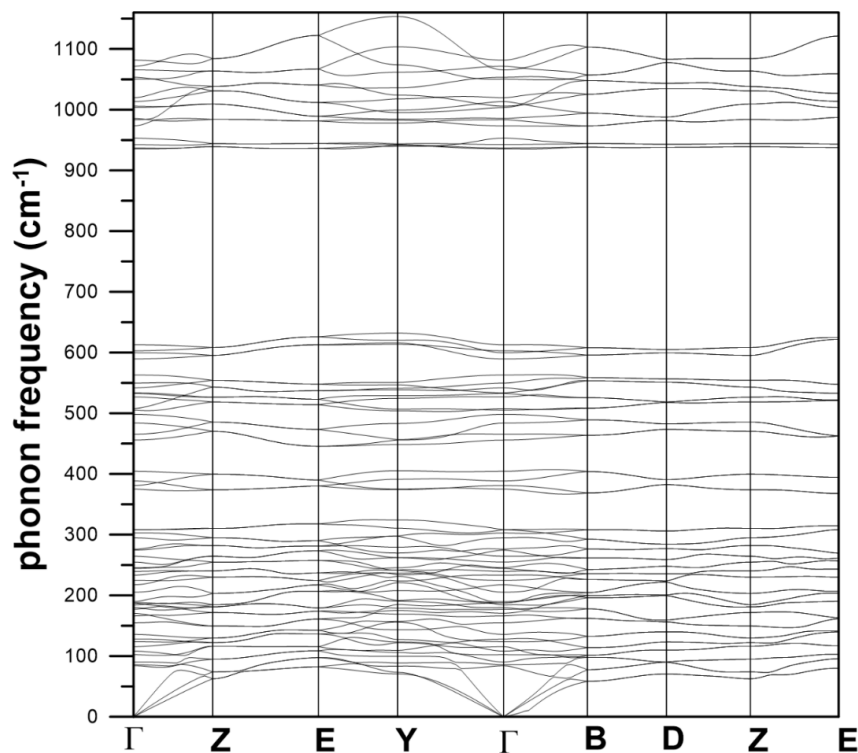


Figure 8. Phonon dispersion along the Brillouin zone of the of monazite-type GdPO_4 .

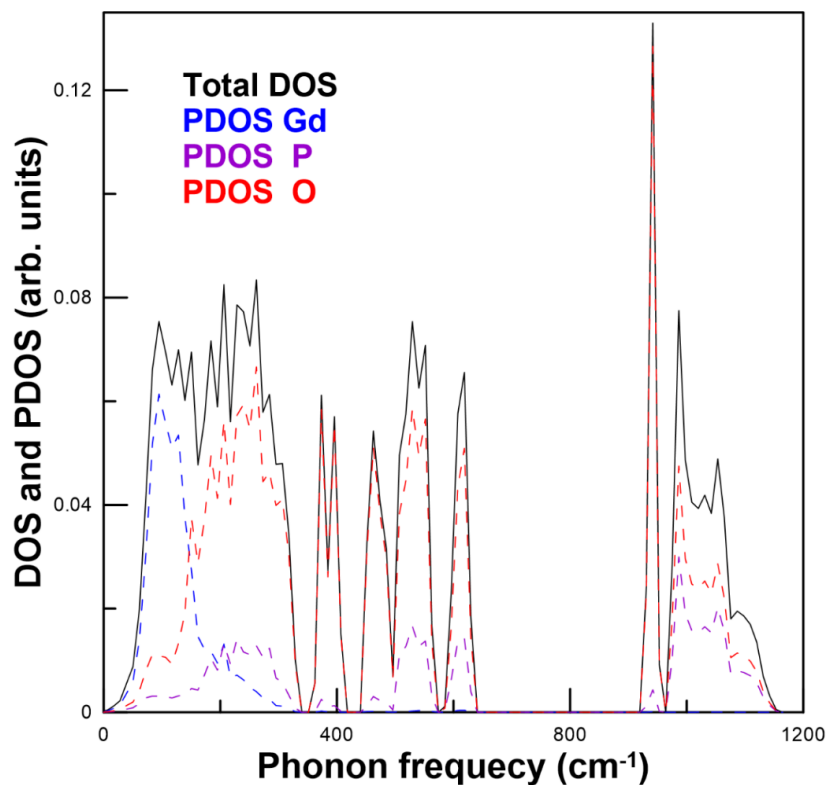


Figure 9. (Color online) Partial and total phonon density of monazite-type GdPO₄ states.

Through group theory analysis, it can be established that the monazite structure has 72 vibrational modes at the zone center: 36 optical Raman-active modes ($18A_g + 18B_g$), 33 optical IR-active modes ($17A_u + 16B_u$), and 3 acoustic modes ($1A_u + 2B_u$). These vibrational modes can be interpreted as 36 internal (ν_1, ν_2, ν_3 and ν_4) and 36 external (translational (T) and rotational (R)) modes [17,63].

The Raman spectrum of many monazite-type phosphates (e.g., BiPO₄, LaPO₄, CePO₄, PrPO₄ and GdPO₄) at ambient conditions has been previously studied by different authors [18,29,64,65]. BiPO₄, LaPO₄, CePO₄, and PrPO₄ have also been studied under compression [17,66–68]. The frequency distribution of Raman modes is very similar for all of them. As in the case of GdPO₄, phonon gaps are observed between the three frequency regions in monazite phosphates; they are also observed in the monazite structure of chromates and selenates [30].

GdPO₄ has a distribution of Raman modes similar to other monazite phosphates [17]. The Raman mode frequencies and their pressure coefficients at room pressure are summarized in Table 6. The mode Grüneisen parameters [69], that provide a dimensionless representation of the response to compression are also reported.

It can be observed that the Raman spectrum of GdPO₄ monazite could be divided into three regions: the low-frequency region, up to 310.91 cm⁻¹, corresponds to the eighteen external or lattice T and R modes ($9A_g + 9B_g$); the medium-frequency region, between 381.30 and 603.46 cm⁻¹, corresponds to the ten internal bending modes ($5A_g + 5B_g$); and the high-frequency region, above 942.72 cm⁻¹, corresponds to the eight internal stretching modes ($4A_g + 4B_g$).

As seen in Figure 10, which shows the theoretical pressure dependence of the Raman-active mode frequencies, most modes harden under compression, as is usual in most materials. However, there are a few modes between 84.78 and 153.94 cm⁻¹ whose frequency changes very slightly under compression.

Table 6. Raman frequencies at ambient pressure, their pressure coefficients, and Grüneisen parameters (γ). The pressure dependence of frequency has been fitted with a second order polynomial: $\omega = \omega_0 + \left(\frac{\partial\omega}{\partial P}\right)P + \left(\frac{\partial^2\omega}{\partial P^2}\right)P^2$.

Mode	ω_0 (cm ⁻¹)	$\frac{\partial\omega}{\partial P}$ (cm ⁻¹ /GPa)	$\frac{\partial^2\omega}{\partial P^2}$ (cm ⁻¹ /GPa ²)	γ
B _g	84.78	0.762	0.0180	1.24
A _g	86.33	0.807	0.0128	1.29
A _g	108.61	0.846	0.0216	1.07
A _g	124.99	0.765	0.008	0.84
B _g	129.32	0.830	0.016	0.88
B _g	137.84	0.852	0.002	0.85
B _g	153.93	0.059	0.027	0.05
A _g	178.30	1.354	0.029	1.05
B _g	180.54	2.610	0.007	1.99
A _g	190.93	1.648	0.016	1.19
A _g	189.67	3.477	0.0343	2.53
B _g	235.29	3.887	0.057	2.28
A _g	240.14	3.014	0.0233	1.736
B _g	246.86	3.411	0.012	1.911
A _g	264.93	5.089	0.069	2.656
B _g	276.56	3.176	0.011	1.588
B _g	295.93	3.982	0.044	1.861
A _g	310.90	2.209	0.000	0.982
B _g	381.29	2.722	0.001	0.987
A _g	404.71	2.524	0.007	0.862
A _g	455.84	2.592	0.018	0.786
B _g	499.31	2.653	0.035	0.734
A _g	506.02	0.589	0.010	0.161
B _g	533.07	1.190	0.017	0.308
A _g	542.17	1.677	0.003	0.427
B _g	563.55	1.750	0.004	0.429
A _g	600.11	1.482	0.007	0.341
B _g	603.45	1.624	0.007	0.372
B _g	942.72	4.215	0.028	0.618
A _g	954.05	4.277	0.036	0.620
A	984.01	4.300	0.013	0.604
A _g	1007.23	5.005	0.039	0.687
B _g	1020.45	3.972	0.016	0.538
A	1051.30	4.269	0.014	0.561
B _g	1055.21	4.837	0.050	0.633
B _g	1072.33	4.480	0.008	0.577

External modes (low frequency region) involve movements of the trivalent Gd atoms, and in phosphate monazites ABO_4 , their frequencies greatly depend on the mass of the A atom [17,70]. These external modes show very different pressure coefficients, since they involve different Gd-O bonds, with different compressibility, as seen in Section 2 [14]. Due to the marked differences between the pressure dependence of the different modes, see Table 6, crossing and anti-crossing phenomena are observed in this region. In particular, one of the modes most affected by compression is the A_g mode at 264.93 cm⁻¹; The lowest-frequency B_g mode is almost not affected by pressure. In previous studies of monazite chromates [37] and phosphates [17], softening of the lower Raman modes was related to a pressure-driven instability of the monazite structure, which could result in a phase transition above 30 GPa [17]. In the case of the monazite-type GdPO₄, the lower modes are little affected by compression. As commented in a previous section, the extension of the simulation up to 60 GPa does not show evidence of soft phonons mode at the Γ point. The pressure-driven instability seems to be related to mechanical instability, rather than dynamical instability.

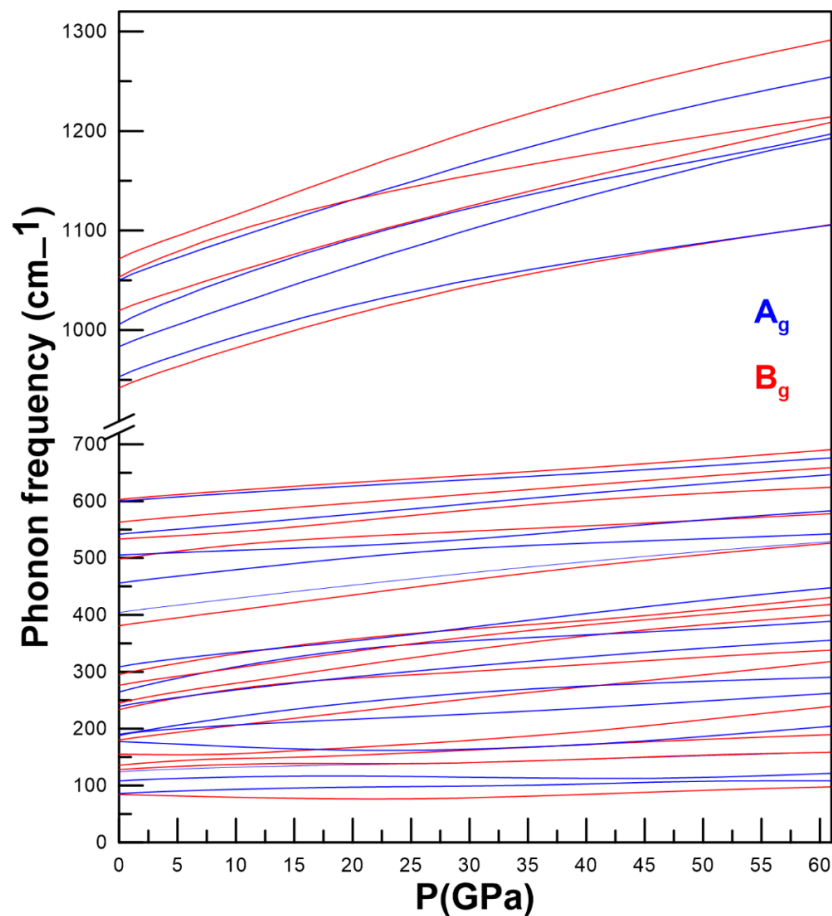


Figure 10. (Color online) Pressure dependence of the Raman modes of monazite-type GdPO₄.

Internal bending motions of the PO₄ tetrahedron (medium frequencies region) have smaller pressure coefficients. Two modes with frequencies A_g = 506.02 and B_g = 530 cm⁻¹ at room pressure are the less affected by pressure, while the mode most sensitive to pressure in this region is the B_g mode with a frequency 381.30 cm⁻¹ at room pressure. The crossover of B_g (499.32 cm⁻¹) and A_g (506.02 cm⁻¹) modes is observed at ≈4 GPa in Figure 10, due to the different pressure dependences. This behavior could be related to the non-isotropic compression of monazite. This can cause the lower-frequency B_g mode to move faster towards high frequencies than the higher-frequency mode.

The internal stretching modes (high frequency region) of the PO₄ tetrahedron have similar pressure coefficients, and they are among the modes whose frequency increases faster under compression.

Regarding the infrared modes of monazite GdPO₄, low-, medium-, and high frequencies modes have the same general behavior with pressure than the Raman modes have. This also happens for monazite chromates [34]. In particular, the modes less affected by pressure is the first A_u mode (91.057 cm⁻¹); see Table 7 and Figure 11.

Table 7. Infrared frequencies at ambient pressure, their pressure coefficients, and Grüneisen parameters (γ). The pressure dependence of frequency has been fitted with a second order polynomial: $\omega = \omega_0 + \left(\frac{\partial\omega}{\partial P}\right)P + \left(\frac{\partial^2\omega}{\partial P^2}\right)P^2$.

Mode	ω_0 (cm ⁻¹)	$\frac{\partial\omega}{\partial P}$ (cm ⁻¹ /GPa)	$\frac{\partial^2\omega}{\partial P^2}$ (cm ⁻¹ /GPa ²)	γ
Au	91.05	0.219	0.007	0.332
Bu	102.50	1.442	0.005	1.946
Au	116.32	1.541	0.0125	1.832
Bu	168.18	0.722	0.013	0.594
Au	170.55	0.866	0.010	0.702
Bu	187.21	1.270	0.032	0.938
Au	189.765	2.761	0.041	2.012
Bu	205.99	2.328	0.021	1.563
Au	219.28	1.386	0.006	0.874
Bu	225.70	3.603	0.026	2.207
Au	245.96	3.397	0.032	1.910
Bu	254.49	3.153	0.013	1.713
Au	274.99	3.789	0.0231	1.905
Au	304.38	4.034	0.039	1.832
Bu	309.61	1.867	0.006	0.834
Bu	375.28	3.061	0.033	1.128
Au	388.32	2.186	0.0011	0.778
Au	466.32	1.013	0.0122	0.300
Bu	484.23	1.851	0.003	0.528
Au	507.73	1.501	0.0044	0.408
Bu	526.89	2.3165	0.0124	0.608
Au	533.09	1.864	0.0033	0.483
Bu	550.13	1.428	0.007	0.359
Bu	590.07	1.384	0.006	0.324
Au	613.26	1.765	0.008	0.398
Au	935.32	4.083	0.023	0.603
Bu	936.86	4.205	0.029	0.620
Au	974.23	3.643	0.017	0.517
Bu	986.50	3.483	0.014	0.488
Bu	1004.66	4.674	0.030	0.643
Au	1014.56	5.209	0.038	0.710
Bu	1066.28	4.956	0.024	0.642
Au	1082.61	4.763	0.024	0.608

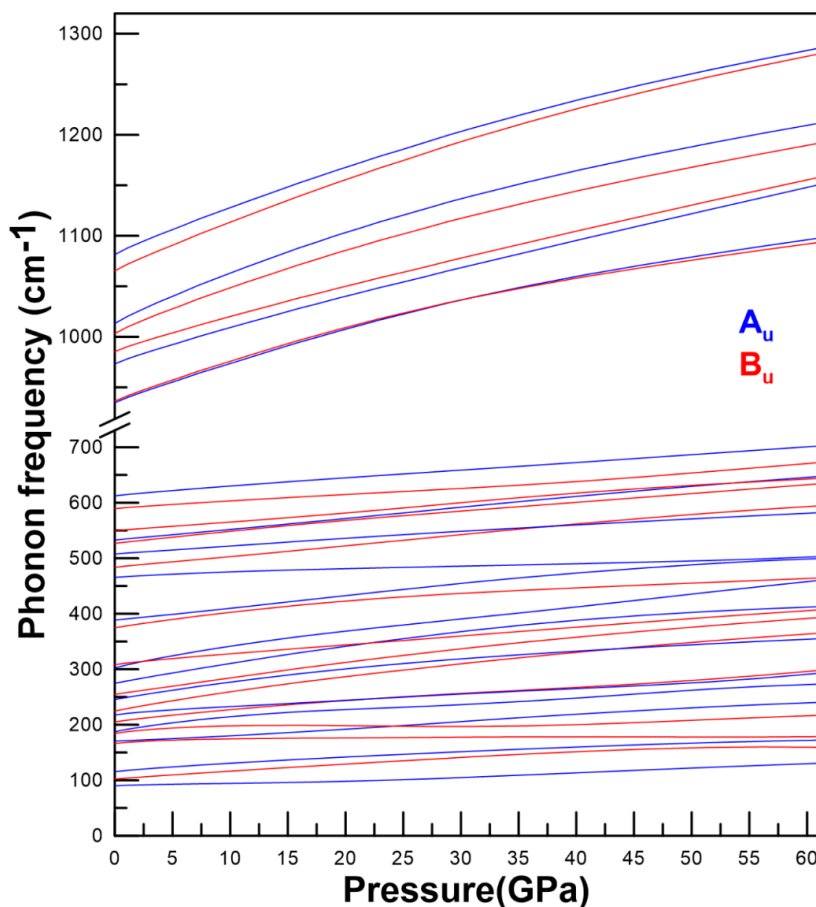


Figure 11. (Color online) Pressure dependence of the infrared modes of monazite-type GdPO_4 .

The Grüneisen parameters in the high frequency region are very similar, while there are large differences between the Grüneisen parameters for the lower frequencies (Tables 6 and 7). Therefore, there are large differences between the restoring force on the atoms associated with the lowest modes.

4. Conclusions

The effects of high pressure on the structure of monazite-type GdPO_4 were studied from first principles, *ab initio* calculations. The simulations were extended up to 60 GPa, well above the maximum experimental pressure previously reported (30 GPa). The evolution of the lattice parameters under compression, the equations of state, and the axial and polyhedral compressibilities are reported. Moreover, the under-pressure distortion of the polyhedral units PO_4 and GdO_9 is shown. The compression of monazite-type GdPO_4 is not isotropic, and the GdO_9 polyhedra account for almost all the volume reduction under pressure.

The elastic constants and elastic stiffness coefficients were accurately determined, through which the elastic behavior of monazite-type GdPO_4 at high pressure was analyzed. The evolution with pressure of the B , G , and E elastic moduli, ν Poisson's ratio, and the B/G ratio was reported. At all pressures, this compound has shown to be ductile and more resistive to volume compression than to shear deformation ($B > G$). Furthermore, the high-pressure mechanical stability of this monoclinic compound was studied. It was found that monazite-type GdPO_4 becomes mechanically unstable above 54 GPa.

Finally, through the total and partial density of states, the contribution of each polynomial units to the vibrational modes was discussed. This contribution is similar to that found in other monazite phosphates. The evolution of the Raman- and infrared active modes of the monazite-type GdPO_4

as function of pressure was analyzed. No soft-modes were found up to 60 GPa at the center of the Brillouin zone.

A possible pressure-driven phase transition or amorphization might occur due to mechanical instability at the high pressure of 54 GPa. No dynamical instability was found up to this pressure.

The results of the presents study confirm the high stability under pressure of the monazite-type GdPO_4 , which is very promising for practical applications.

Author Contributions: Both authors contributed equally to this work: simulations, analysis and interpretation of results and writing of the manuscript.

Acknowledgments: Research supported by the Spanish Ministerio de Economía y Competitividad, the Spanish Research Agency, and the European Fund for Regional Development under Grant Nos. MAT2016-75586-C4-3-P. We acknowledge the computer time provided by the RES (Red Española de Supercomputación) and the MALTA cluster.

Conflicts of Interest: The authors declare no conflict of interest.

References

1. Ni, Y.X.; Hughes, J.M.; Mariano, A.N. Crystal-chemistry of the monazite and xenotime structures. *Am. Mineral.* **1995**, *80*, 21–26. [[CrossRef](#)]
2. Morgan, P.E.D.; Marshall, D.B. Ceramic compounds of monazite and alumina. *J. Am. Ceram. Soc.* **1995**, *78*, 1553–1563. [[CrossRef](#)]
3. Kolitsch, U.; Holtstam, D. Crystal chemistry of REEXO₄ compounds (X = P, As, V). II. Review of REEXO₄ compounds and their stability fields. *Eur. J. Mineral.* **2004**, *16*, 117–126. [[CrossRef](#)]
4. Kaminskii, A.A.; Bettinelli, M.; Speghini, A.; Rhee, H.; Eichler, H.J.; Mariotto, G. Tetragonal YPO₄—A novel SRS-active crystal. *Laser Phys. Lett.* **2008**, *5*, 367–374. [[CrossRef](#)]
5. Clavier, N.; Podor, R.; Dacheux, N. Crystal chemistry of the monazite structure. *J. Eur. Ceram. Soc.* **2011**, *31*, 941–976. [[CrossRef](#)]
6. Errandonea, D. High-pressure phase transitions and properties of MTO₄ compounds with the monazite-type structure. *Phys. Status Solidi B Basic Solid State Phys.* **2017**, *254*, 1700016. [[CrossRef](#)]
7. Rubatto, D.; Hermann, J.; Buick, I.S. Temperature and bulk composition control on the growth of monazite and zircon during low-pressure anatexis (Mount Stafford, central Australia). *J. Petrol.* **2006**, *47*, 1973–1996. [[CrossRef](#)]
8. Grove, M.; Harrison, T.M. Monazite Th-Pb age depth profiling. *Geology* **1999**, *27*, 487–490. [[CrossRef](#)]
9. Meldrum, A.; Boatner, L.A.; Ewing, R.C. Displacive radiation effects in the monazite- and zircon-structure orthophosphates. *Phys. Rev. B* **1997**, *56*, 13805–13814. [[CrossRef](#)]
10. Ewing, R.C. The design and evaluation of nuclear-waste forms: Clues from mineralogy. *Can. Mineral.* **2001**, *39*, 697–715. [[CrossRef](#)]
11. Mullica, D.F.; Gossie, D.A.; Boatner, L.A. Coordination geometry and structural determinations of SmPO₄, EuPO₄ and GdPO₄. *Inorg. Chim. Acta F* **1985**, *109*, 105–110. [[CrossRef](#)]
12. Neumeier, S.; Arinicheva, Y.; Ji, Y.; Heuser, J.M.; Kowlaski, P.M.; Kegler, P.; Sclenz, H.; Bosbach, D.; Deissmann, G. New insights into phosphate based material for the immobilization of actinides. *Radiochim. Acta* **2017**, *105*, 961–984.
13. Lessing, P.A.; Erickson, A.W. Synthesis and characterization of gadolinium phosphate neutron absorber. *J. Eur. Ceram. Soc.* **2003**, *23*, 3049–3057. [[CrossRef](#)]
14. Lacombe-Perales, R.; Errandonea, D.; Meng, Y.; Bettinelli, M. High-pressure stability and compressibility of APO(4) (A = La, Nd, Eu, Gd, Er, and Y) orthophosphates: An x-ray diffraction study using synchrotron radiation. *Phys. Rev. B* **2010**, *81*, 064113. [[CrossRef](#)]
15. Errandonea, D.; Gomis, O.; Santamaria-Perez, D.; Garcia-Domene, B.; Munoz, A.; Rodriguez-Hernandez, P.; Achary, S.N.; Tyagi, A.K.; Popescu, C. Exploring the high-pressure behavior of the three known polymorphs of BiPO₄: Discovery of a new polymorph. *J. Appl. Phys.* **2015**, *117*, 105902. [[CrossRef](#)]
16. Achary, S.N.; Bevara, S.; Tyagi, A.K. Recent progress on synthesis and structural aspects of rare-earth phosphates. *Coord. Chem. Rev.* **2017**, *340*, 266–297. [[CrossRef](#)]

17. Errandonea, D.; Gomis, O.; Rodriguez-Hernandez, P.; Munoz, A.; Ruiz-Fuertes, J.; Gupta, M.; Achary, S.N.; Hirsch, A.; Manjon, F.J.; Peters, L.; et al. High-pressure structural and vibrational properties of monazite-type BiPO_4 , LaPO_4 , CePO_4 , and PrPO_4 . *J. Phys. Condens. Matter*. **2018**, *30*, 065401. [[CrossRef](#)] [[PubMed](#)]
18. Heffernan Karina, M.; Ross, N.L.; Spencer, E.C.; Boatner, L.A. The structural response of gadolinium phosphate to pressure. *J. Solid State Chem.* **2016**, *241*, 180–186. [[CrossRef](#)]
19. Wilkinson, T.M.; Wu, D.; Musselman, M.A.; Li, N.; Mara, N.; Packard, C.E. Mechanical behavior of rare-earth orthophosphates near the monazite/xenotime boundary characterized by nanoindentation. *Mater. Sci. Eng. A* **2017**, *691*, 203–210. [[CrossRef](#)]
20. Feng, J.; Xiao, B.; Zhou, R.; Pan, W. Anisotropy in elasticity and thermal conductivity of monazite-type REPO_4 (RE = La, Ce, Nd, Sm, Eu and Gd) from first-principles calculations. *Acta Mater.* **2013**, *61*, 7364–7383. [[CrossRef](#)]
21. Rustad, J.R. Density functional calculation of enthalpies of formation of rare-earth orthophosphates. *Am. Mineral.* **2012**, *97*, 791–799. [[CrossRef](#)]
22. Li, Y.; Kowalski, P.M.; Blanca-Romero, A.; Vinograd, V.; Bosbach, D. Ab initio calculation of excess properties of $\text{La}_{1-x}(\text{Ln}, \text{An})_x\text{PO}_4$ solid solutions. *J. Sol. State Chem.* **2014**, *220*, 137–141. [[CrossRef](#)]
23. Kowalski, P.M.; Beridze, G.; Vinograd, V.L.; Bosbach, D. Heat capacities of lanthanides and actinide monazite-type ceramics. *J. Nucl. Mater.* **2015**, *464*, 147–154. [[CrossRef](#)]
24. Kowalski, P.M.; Li, Y. Relationship between the thermodynamic excess properties of mixing and the elastic moduli in the monazite-type ceramics. *J. Eur. Ceram. Soc.* **2016**, *36*, 2093–2096. [[CrossRef](#)]
25. Gomis, O.; Lavina, B.; Rodriguez-Hernandez, P.; Munoz, A.; Errandonea, R.; Errandonea, D.; Bettinelli, M. High-pressure structural, elastic, and thermodynamic properties of zircon-type HoPO_4 and TmPO_4 . *J. Phys. Condens. Matter*. **2017**, *29*, 095401. [[CrossRef](#)] [[PubMed](#)]
26. Errandonea, D.; Pellicer-Porres, J.; Martinez-Garcia, D.; Ruiz-Fuertes, J.; Friedrich, A.; Morgenroth, W.; Popescu, C.; Rodriguez-Hernandez, P.; Munoz, A.; Bettinelli, M. Phase Stability of Lanthanum Orthovanadate at High Pressure. *J. Phys. Chem. C* **2016**, *120*, 13749–13762. [[CrossRef](#)]
27. Errandonea, D.; Munoz, A.; Rodriguez-Hernandez, P.; Gomis, O.; Achary, S.N.; Popescu, C.; Patwe, S.J.; Tyagi, A.K. High-Pressure Crystal Structure, Lattice Vibrations, and Band Structure of BiSbO_4 . *Inorg. Chem.* **2016**, *55*, 4958–4969. [[CrossRef](#)] [[PubMed](#)]
28. Errandonea, D.; Garg, A.B. Recent progress on the characterization of the high-pressure behaviour of AVO_4 orthovanadates. *Prog. Mater. Sci.* **2018**, *97*, 123–169. [[CrossRef](#)]
29. Achary, S.N.; Errandonea, D.; Munoz, A.; Rodriguez-Hernandez, P.; Manjon, F.J.; Krishna, P.S.R.; Patwe, S.J.; Grover, V.; Tyagi, A.K. Experimental and theoretical investigations on the polymorphism and metastability of BiPO_4 . *Dalton Trans.* **2013**, *42*, 14999–15015. [[CrossRef](#)] [[PubMed](#)]
30. Errandonea, D.; Munoz, A.; Rodriguez-Hernandez, P.; Proctor, J.E.; Sapina, F.; Bettinelli, M. Theoretical and experimental study of the crystal structures, lattice vibrations, and band structures of monazite-type PbCrO_4 , PbSeO_4 , SrCrO_4 , and SrSeO_4 . *Inorg. Chem.* **2015**, *54*, 7524–7535. [[CrossRef](#)] [[PubMed](#)]
31. Hohenberg, P.; Kohn, W. Inhomogeneous electron gas. *Phys. Rev. B* **1964**, *136*, B864–B871. [[CrossRef](#)]
32. Kresse, G.; Furthmüller, J. Efficiency of ab-initio total energy calculations for metals and semiconductors using a plane-wave basis set. *Comput. Mater. Sci.* **1996**, *6*, 15–50.
33. Kresse, G.; Hafner, J. Ab-Initio molecular-dynamics simulation of the liquid-metal amorphous-semiconductor transition in germanium. *Phys. Rev. B* **1994**, *49*, 14251–14269. [[CrossRef](#)]
34. Kresse, G.; Hafner, J. Ab initio molecular-dynamics for liquid-metals. *Phys. Rev. B* **1993**, *47*, 558–561. [[CrossRef](#)]
35. Blöchl, P.E. Projector augmented-wave method. *Phys. Rev. B* **1994**, *50*, 17953–17979. [[CrossRef](#)]
36. Kresse, G.; Joubert, D. From ultrasoft pseudopotentials to the projector augmented-wave method. *Phys. Rev. B* **1999**, *59*, 1758–1775. [[CrossRef](#)]
37. Gleissner, J.; Errandonea, D.; Segura, A.; Pellicer-Porres, J.; Hakeem, M.A.; Proctor, J.E.; Raju, S.V.; Kumar, R.S.; Rodriguez-Hernandez, P.; Munoz, A.; et al. Monazite-type SrCrO_4 under compression. *Phys. Rev. B* **2016**, *94*, 134108. [[CrossRef](#)]
38. Perdew, J.P.; Ruzsinszky, A.; Csonka, G.I.; Vydrov, O.A.; Scuseria, G.E.; Constantin Lucian, A.; Zhou, X.; Burke, K. Restoring the density-gradient expansion for exchange in solids and surfaces. *Phys. Rev. Lett.* **2008**, *100*, 136406. [[CrossRef](#)] [[PubMed](#)]

39. Monkhorst, H.J.; Pack, J.D. Special points for Brillouin-zone integrations. *Phys. Rev. B* **1976**, *13*, 5188–5192. [[CrossRef](#)]
40. Mujica, A.; Rubio, A.; Munoz, A.; Needs, R.J. High-pressure phases of group-IV, III-V, and II-VI compounds. *Rev. Mod. Phys.* **2013**, *75*, 863–912. [[CrossRef](#)]
41. Nielsen, O.H.; Martin, R.M. Quantum-mechanical theory of stress and force. *Phys. Rev. B* **1985**, *32*, 3780–3791. [[CrossRef](#)]
42. Chetty, N.; Munoz, A.; Martin, R.M. 1st-principles calculation of the elastic-constants of AlAs. *Phys. Rev. B* **1989**, *40*, 11934–11936. [[CrossRef](#)]
43. Le Page, Y.; Saxe, P. Symmetry-general least-squares extraction of elastic data for strained materials from ab initio calculations of stress. *Phys. Rev. B* **2002**, *65*, 104104. [[CrossRef](#)]
44. Parlinski, K. Computer Code Phonon. Available online: <http://www.computingformaterials.com/> (accessed on 14 July 2014).
45. Blanca-Romero, A.; Kowalski, P.M.; Beridze, G.; Schlenz, H.; Bosbach, D. Performance of DFT plus U Method for Prediction of Structural and Thermodynamic Parameters of Monazite-Type Ceramics. *J. Comput. Chem.* **2014**, *35*, 1339–1346. [[CrossRef](#)] [[PubMed](#)]
46. Birch, F. Finite elastic strain of cubic crystals. *Phys. Rev.* **1947**, *71*, 809–824. [[CrossRef](#)]
47. Du, A.; Wan, C.; Qu, Z.; Pan, W. Thermal Conductivity of Monazite-Type REPO₄ (RE = La, Ce, Nd, Sm, Eu, Gd). *J. Am. Ceram. Soc.* **2009**, *92*, 2687–2692. [[CrossRef](#)]
48. Li, H.; Zhang, S.; Zhou, S.; Cao, X. Bonding Characteristics, Thermal Expansibility, and Compressibility of RXO₄ (R = Rare Earths, X = P, As) within Monazite and Zircon Structures. *Inorg. Chem.* **2009**, *48*, 4542–4548. [[CrossRef](#)] [[PubMed](#)]
49. Momma, K.; Izumi, F. VESTA 3 for three-dimensional visualization of crystal, volumetric and morphology data. *J. Appl. Crystallogr.* **2011**, *44*, 1272–1276. [[CrossRef](#)]
50. Nye, J.F. *Physical Properties of Crystals. Their Representation by Tensor and Matrices*; Oxford University Press: Oxford, UK, 1957.
51. Wallace, D.C. *Thermodynamics of Crystals*; Dover Publications: New York, NY, USA, 1998.
52. Grimvall, G.; Magyari-Koepe, B.; Ozolins, V.; Persson, K.A. Lattice instabilities in metallic elements. *Rev. Mod. Phys.* **2012**, *84*, 945–986. [[CrossRef](#)]
53. Born, M.; Huang, K. *Dynamical Theory of Crystal Lattices*; Clarendon Press: London, UK, 1954.
54. Wallace, D.C. Thermoelasticity of stressed materials and comparison of various elastic constants. *Phys. Rev.* **1967**, *162*, 776–789. [[CrossRef](#)]
55. Voigt, W. *Lehrbuch der Kristallphysik (mit Ausschluss der Kristalloptik)*; B.G. Teubner: Leipzig/Berlin, Germany, 1928.
56. Reuss, A. Berechnung der Fließgrenze von Mischkristallen auf Grund der Plastizitätsbedingung für Einkristalle. *J. Appl. Math. Mech.* **1929**, *9*, 49–58. [[CrossRef](#)]
57. Hill, R. The elastic behaviour of a crystalline aggregate. *Proc. Phys. Soc. Lond.* **1952**, *65*, 349–355. [[CrossRef](#)]
58. Zhao, X.S.; Shang, S.L.; Liu, Z.K.; Shen, J.Y. Elastic properties of cubic, tetragonal and monoclinic ZrO₂ from first-principles calculations. *J. Nucl. Mater.* **2011**, *415*, 13–17. [[CrossRef](#)]
59. Caracas, R.; Ballaran, T.B. Elasticity of (K, Na)AlSi₃O₈ hollandite from lattice dynamic calculations. *Phys. Earth Planet. Inter.* **2010**, *181*, 21–26. [[CrossRef](#)]
60. Brazhkin, V.V.; Lyapin, A.G.; Hemley, R.J. Harder than diamond: Dreams and reality. *Philos. Mag. A* **2002**, *82*, 231–253. [[CrossRef](#)]
61. Greaves, G.N.; Greer, A.L.; Lakes, R.S.; Rouxel, T. Poisson's ratio and modern materials. *Nat. Mater.* **2011**, *10*, 823–837. [[CrossRef](#)] [[PubMed](#)]
62. Pugh, S.F. Relations between the elastic moduli and the plastic properties of polycrystalline pure metals. *Philos. Mag.* **1954**, *45*, 823–843. [[CrossRef](#)]
63. Silva, E.N.; Ayala, A.P.; Guedes, I.; Paschoal, C.W.A.; Moreira, R.L.; Loong, C.K.; Boatner, L.A. Vibrational spectra of monazite-type rare-earth orthophosphates. *Opt. Mater.* **2006**, *29*, 224–230. [[CrossRef](#)]
64. Begun, G.M.; Beall, G.W.; Boatner, L.A.; Gregor, W.J. Raman-spectra of the rare-earth ortho-phosphates. *J. RAMAN Spectrosc.* **1981**, *11*, 273–278. [[CrossRef](#)]
65. Ruschel, K.; Nasdala, L.; Kronz, A.; Hanchar, J.M.; Toebbens, D.M.; Skoda, R.; Finger, F.; Moeller, A. A Raman spectroscopic study on the structural disorder of monazite-(Ce). *Mineral. Petrol.* **2012**, *105*, 41–55. [[CrossRef](#)]

66. Huang, T.; Lee, J.S.; Kung, J.; Lin, C.M. Study of monazite under high pressure. *Solid State Commun.* **2010**, *150*, 1845–1850. [[CrossRef](#)]
67. Zhao, Z.; Zhang, X.; Zuo, J.A.; Ding, Z.J. Pressure effect on optical properties and structure stability of LaPO₄:Eu³⁺ Microspheres. *J. Nanosci. Nanotechnol.* **2010**, *10*, 7791–7794. [[CrossRef](#)] [[PubMed](#)]
68. Zhao, Z.; Zuo, J.A.; Ding, Z.J. Pressure effect on optical properties and structure stability of LaPO₄:Eu³⁺ hollow spheres. *J. Rare Earths* **2010**, *28*, 254–257. [[CrossRef](#)]
69. Grüneisen, E. Concerning the thermic expansion of metals. *Ann. Phys.* **1910**, *33*, 33–64. [[CrossRef](#)]
70. Ruiz-Fuertes, J.; Errandonea, D.; Lopez-Moreno, S.; Gonzalez, J.; Gomis, O.; Vilaplana, R.; Manjon, F.J.; Munoz, A.; Rodriguez-Hernandez, P.; Friedrich, A.; et al. High-pressure Raman spectroscopy and lattice-dynamics calculations on scintillating MgWO₄: Comparison with isomorphous compounds. *Phys. Rev. B* **2011**, *83*, 214112. [[CrossRef](#)]



© 2018 by the authors. Licensee MDPI, Basel, Switzerland. This article is an open access article distributed under the terms and conditions of the Creative Commons Attribution (CC BY) license (<http://creativecommons.org/licenses/by/4.0/>).